

Formation and Dynamics of a Long-Lived Eddy Train in the South China Sea: A Modeling Study

ZHONGYA CAI AND JIANPING GAN

Department of Mathematics, and Environmental Science Programs, Hong Kong University of Science and Technology, Kowloon, Hong Kong, China

(Manuscript received 4 January 2017, in final form 28 August 2017)

ABSTRACT

A process-oriented numerical modeling study was conducted to investigate the formation and underlying forcing of an anticyclonic eddy train observed in the northern South China Sea. Observations showed that long-lived anticyclonic eddies formed an eddy train along an eastward separated jet across the northern South China Sea in summer. The eddy train plays a critical role in regulating ocean circulation in the region. Forced by the southwesterly monsoon and prevailing dipole wind stress curl in the summer, the northward coastal jet separates from the west boundary of the South China Sea basin and overshoots northeastward into the basin. The anticyclonic recirculation of the separated jet forms the first anticyclonic eddy in the eddy train. The jet meanders downstream with a strong negative shear vorticity that forms a second and a third anticyclonic eddy along the jet's path. These three eddies form the eddy train. These eddies weaken gradually with depth from surface, but they can extend to approximately 500 m deep. The inherent stratification in the region regulates the three-dimensional scale of the anticyclonic eddies and constrains their intensity vertical extension by weakening the geostrophic balance within these eddies. Analyses of the vorticity balance indicate that the eddy train's negative vorticity originates from the beta effect of northward western boundary current and from the subsequent downstream vorticity advection in the jet. The jet separation is a necessary condition for the formation of the eddy train, and the enhanced stratification, increased summer wind stress, and associated negative wind stress curl are favorable conditions for the formation of the anticyclonic eddies.

1. Introduction

The South China Sea (SCS) is the largest marginal sea in the tropics (Fig. 1). It is connected to the East China Sea by Taiwan Strait. Luzon Strait (LS) connects the SCS to the Pacific Ocean. The Mindoro Strait (MS) connects the SCS to the Sulu Sea, and Karimata Strait (KS) connects it to the Java Sea.

The upper-layer circulation in the SCS is strongly influenced by seasonal Asian monsoons and by the Kuroshio intrusion in its northern part through LS (Qu 2000; Su 2004; Xue et al. 2004; Gan et al. 2006; Fang et al.

2009; Qu et al. 2009; Xu and Oey 2015; Gan et al. 2016a). The winter/summer monsoon drives a southwestward/northeastward current over the broad continental margin in the northern and western SCS. The separation of the strong western boundary current characterizes the circulation on the west side of the basin, while the current on the east side is weaker (Gan and Qu 2008). Water from the western Pacific Ocean enters the SCS through LS and moves southward, exiting the basin through KS and MS (Gan et al. 2016b).

The SCS has mesoscale eddies that influence the dynamics in the basin and play an important role in heat and salt transport (Chen et al. 2012). These eddies have been extensively studied using hydrographic data (e.g., Wang et al. 2008; Cheng and Qi 2010; Hu et al. 2011, 2012; Zhang et al. 2013, 2016) and numerical models (e.g., Wu and Chiang 2007; Wang and Gan 2014; Lin et al. 2015; Sun et al. 2016). In the northern SCS (NSCS), long-lived eddies in the region have been reported (Nan et al. 2011a; Zheng et al. 2014; Chu et al. 2014). The higher eddy kinetic energy is found to the east of Vietnam and southwest of Taiwan (Chen et al. 2009), where

Denotes content that is immediately available upon publication as open access.

Supplemental information related to this paper is available at the Journals Online website: <https://doi.org/10.1175/JPO-D-17-0002.s1>.

Corresponding author: Jianping Gan, magan@ust.hk

DOI: 10.1175/JPO-D-17-0002.1

© 2017 American Meteorological Society. For information regarding reuse of this content and general copyright information, consult the [AMS Copyright Policy](#) (www.ametsoc.org/PUBSReuseLicenses).

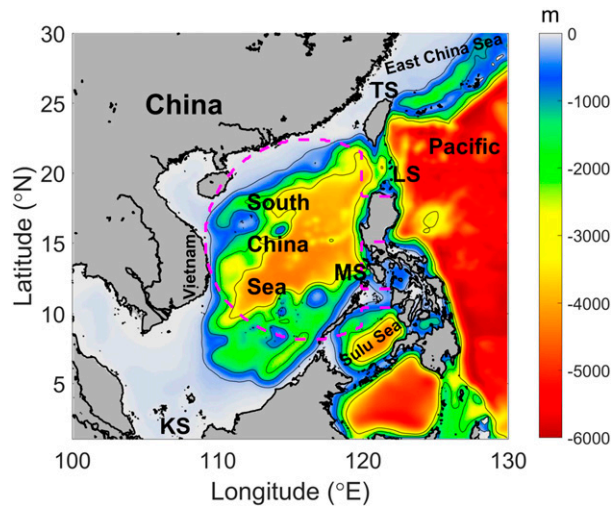


FIG. 1. Location and bathymetry (m) of the South China Sea, showing Luzon Strait (LS), Taiwan Strait (TS), Mindoro Strait (MS), and Karimata Strait (KS). The dashed purple line shows the shape of the idealized basin.

mesoscale eddies are active (Chen et al. 2011). In addition, the eddies in the SCS are sharply spun down by the baroclinicity within the upper 200–300 m (Hu et al. 2011; Chu et al. 2014; Wang and Gan 2014; Lin et al. 2015), but the signals of eddies can also reach the waters near the bottom in the NSCS (Zhang et al. 2013, 2016).

Nan et al. (2011a) detected an eddy train with three long-lived anticyclonic eddies (AEs) across the NSCS basin in 2007 summer and examined their evolution process. The AEs were formed from west to east sequentially and aligned with an eastward jet around 18°N. The life span of these AEs was months during the summer, which was larger than the average SCS eddy's lifespan of 8.8 weeks (Chen et al. 2011). In addition, Zheng et al. (2014) showed that the positions of these AEs remained almost unchanged for at least 3 weeks. Although the number and birthplace of the AEs in the NSCS varied in different years, the AEs were commonly generated to the right of the separated western boundary current (Nan et al. 2011a).

Current instability, topography, geostrophic turbulence, and diapycnal mixing followed by geostrophic adjustment can all induce eddies (McWilliams 1985). Baroclinic structures and baroclinic instability also influence the formation and evolution of ocean eddies (e.g., Badin et al. 2009; Kawaguchi et al. 2012). Recently, Molemaker et al. (2015) and Gula et al. (2015) have showed the linkages among boundary current separation, instability, and subsequent formation of anticyclones, as a result of current–topography interaction. Wind-wake can also generate eddy in the lee of island (Couvelard et al. 2012; Caldeira et al. 2014).

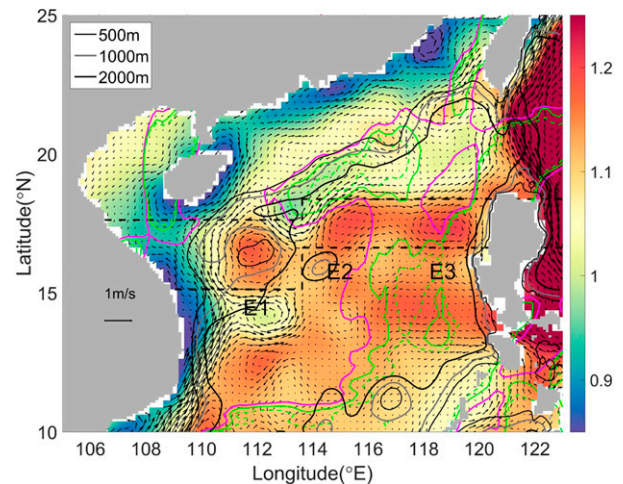


FIG. 2. Absolute dynamic topography (m; color) and surface geostrophic current (m s^{-1} ; vectors) averaged in the summer 2007. The purple solid, green solid, and green dashed lines show the summer-averaged WSC in 2007 with values of 0 , -3×10^{-8} , and $-5 \times 10^{-8} \text{ Pa m}^{-1}$, respectively. Black dashed lines define the north and south boundary of the region with the eddy train. The thick black, gray, and thin black lines are the 500-, 1000-, and 2000-m isobaths, respectively. E1, E2, and E3 represent three AEs in the eddy train.

In the SCS, wind stress curl (WSC) is considered to be important for eddy generation in summer (Chi et al. 1998; Qu 2000; Xiu et al. 2010). The separation of the coastal jet current in summer is the key factor for eddy formation in the southwestern SCS (Gan and Qu 2008; Hu et al. 2011). In the NSCS, AEs can originate from the Kuroshio shedding and associated vorticity advection in the northeastern SCS (Zhang et al. 2016, 2017; Jia and Chassignet 2011; Nan et al. 2011b).

Nan et al. (2011a) suggested that frontal instability of a current was likely to be the most essential factor for the generation of the eddy train, while Zheng et al. (2014) attributed it to the standing wave mode. A complete dynamic rationalization for AEs remains unclear. In particular, explanations for the nature and origin of the force that drives the AEs have never been provided. The objectives of this paper are to investigate the formation and underlying forcing of the long-lived eddy train and the roles of the different forcing factors in the NSCS.

Section 2 of this paper presents the characteristics of the long-lived eddy train and the concurrent oceanic circulation and wind forcing based on satellite remotely sensing data. Section 3 describes the numerical model and its implementation. Section 4 presents the detailed examination of eddy-train formation. We conduct vorticity balance analyses of the eddy train and sensitivity experiments in section 5, and we provide a summary of our findings in section 6.

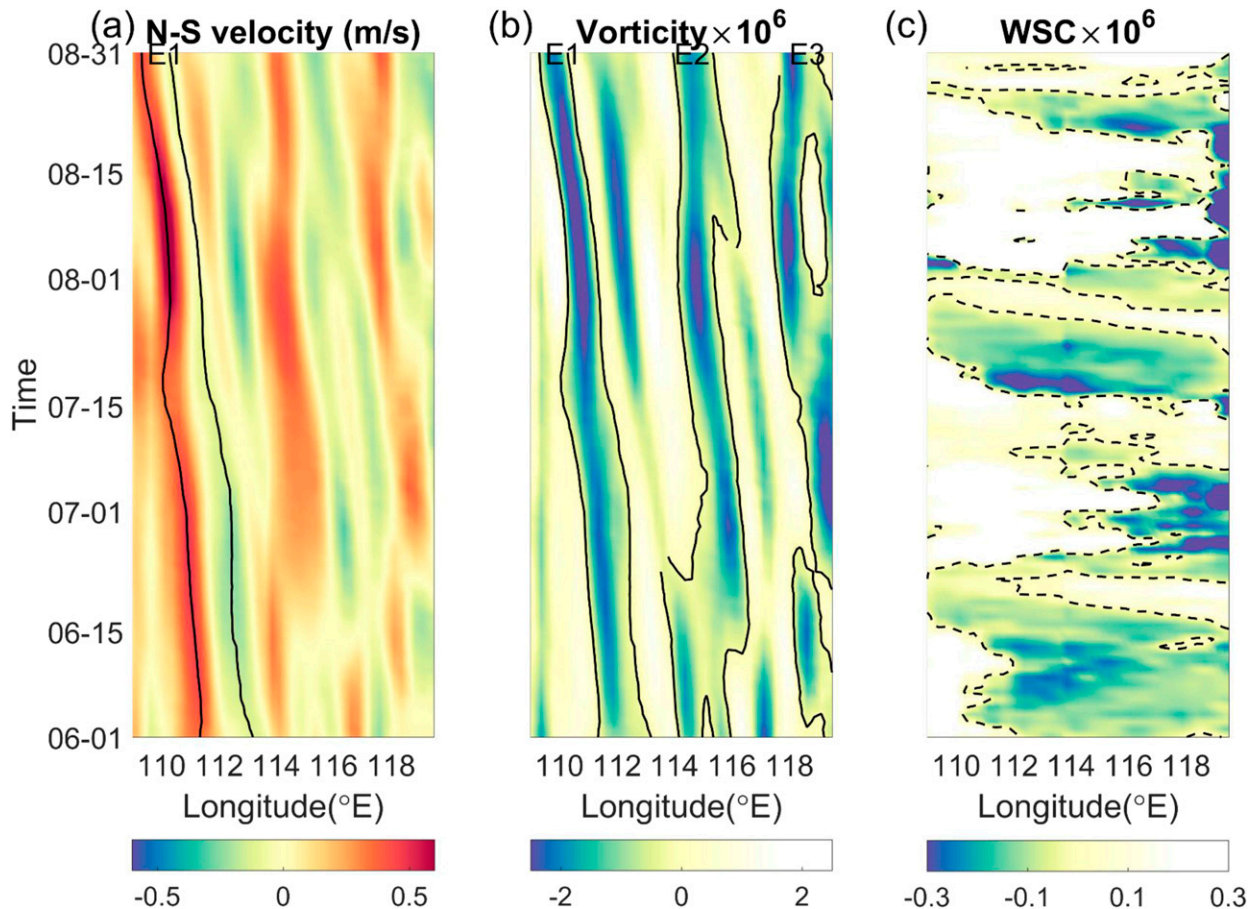


FIG. 3. Time series of meridional surface northward geostrophic (a) velocity (m s^{-1}), (b) vorticity (s^{-1}), and (c) WSC (Pa m^{-1}) as a function of longitude within the zonal band encircling the AEs, as defined by the two black dashed lines in Fig. 2. Black lines in (a) and (b) show the relative vorticity with value of $-2 \times 10^{-7} \text{ s}^{-1}$ and dashed lines in (c) refer to the zero WSC. E1, E2, and E3 represent three AEs in the eddy train.

2. Observations of the eddy train

To examine the basic characteristics of eddy train in the NSCS, we used daily observed absolute dynamic topography (ADT) data and corresponding surface geostrophic current with $1/4^\circ$ resolution, from the Archiving, Validation, and Interpolation of Satellite Oceanographic data project (<ftp.avisioceanobs.com>). The eastward and northward surface geostrophic currents (u and v) are calculated with the equations $u = -(g/f)h_y$ and $v = (g/f)h_x$, where h is the ADT, g is the gravitational acceleration, and f is the Coriolis parameter. We calculated the wind stress (WS) using the $1/4^\circ$ daily reanalysis wind data from the Jet Propulsion Laboratory (<ftp://podaac-ftp.jpl.nasa.gov/>). The WS calculation was based on a bulk formula (Steward 2009).

We chose the eddy train from the summer of 2007 to illustrate the detailed spatial-temporal characteristics (Figs. 2, 3). The basic formation process (Fig. S1 in the supplemental material) is similar to that revealed in a

previous study using sea level anomaly data (Nan et al. 2011a). In 2007, there were three long-lived AEs (E1, E2, and E3) in the NSCS, and they were linked to the separation of the wind-driven northward western boundary current. The separated branch of the western boundary current formed a meandering jet current across the NSCS along 18°N . Three AEs formed an eddy train to the right of the jet current. Among these AEs, E1 was larger and linked to the recirculation of the boundary current separation (Gan and Qu 2008).

There was no obvious direct correlation between WSC and the eddy train in the NSCS. Taking summer 2007 as example, the averaged WSC was negative near E3, but positive in E1 and E2 (Fig. 2). Figure 3 illustrates the links among the WSC, western boundary current, and AEs. Three distinct AEs corresponded to the three alternating northward and southward currents during the summer. Under the influence of a background eastward jet current, these AEs propagated westward slower than a

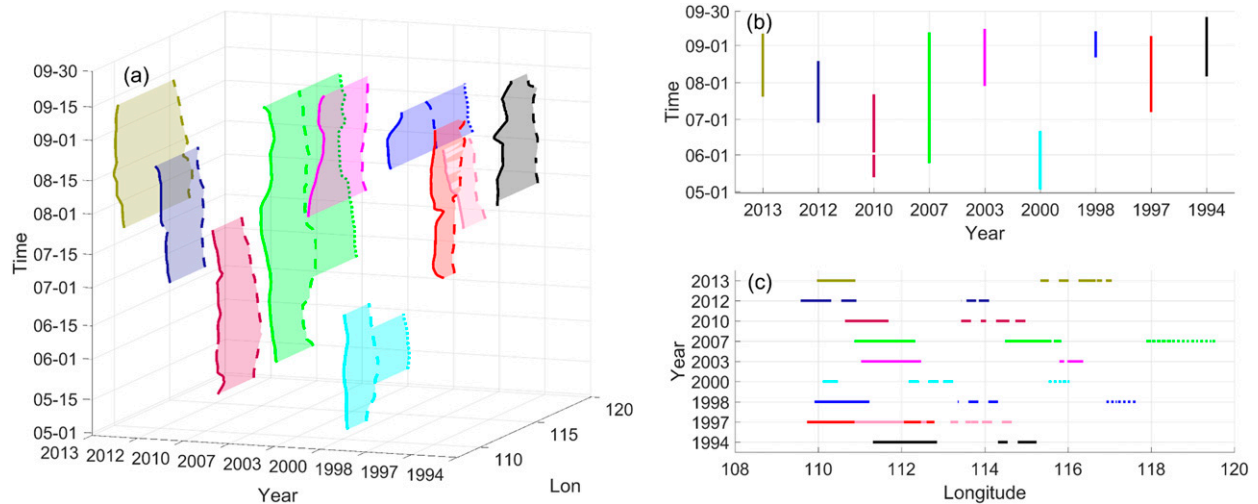


FIG. 4. (a) Time series of eddy train events as a function of longitude in the SCS, (b) lifespan of the eddy train events by viewing along the x axis of panel (a), and (c) spatial movements of AEs in the eddy train events by viewing along the z axis of panel (a). The solid, dashed, and dotted lines show the center of the first, second, and third AE.

first-mode baroclinic Rossby wave, which can cross the basin in less than 4 months (Liu et al. 2001). All these observational evidences and previous studies suggest that the longest-lived anticyclone was initiated on the western side of the SCS and that an eddy train is formed in summer 2007 along the separated jet with a stationary/limited propagation speed. We expect that the boundary current separation and the separated jet itself form the eddy trains. The underlying dynamic processes of the eddy train are investigated in this study.

Figure 4 shows the spatial-temporal variation of the AEs over 23 years from 1993 to 2015 based on an eddy tracking method (<https://sourceforge.net/projects/eddydetect/>). Since the eddy trains were mainly oriented eastward or northwestward (Fig. S2), we used longitude to show the location and movement of AEs. We only select the strong, long-lived eddy train events with at least two AEs and lifespan generally longer than 1 month after the formation of the second AE. When including those events with lifespan less than 2 weeks, the eddy train existed in most of the summers during all these years. The formation time, lifespan, location, and spatial scale of AEs vary in different years, but all of them are related to the boundary current separation and formed along separated jet. Thus, the eddy train formed by the separated boundary current constantly occurred in the SCS.

3. Numerical ocean model description and implementation

We used the Princeton Ocean Model (Blumberg and Mellor 1987) to conduct a process-oriented, three-

dimensional, time-dependent simulation governed by the hydrostatic primitive equations. In the vertical mixing parameterization, we adopted a local closure scheme based on the level-2.5 turbulent kinetic energy equations by Mellor and Yamada (1982). To isolate the physical processes better and to identify the invoked forcing mechanisms of the eddy train formation, we adopted an idealized geometry that preserved the spatial scale and characteristics of the real SCS for the formation of the eddy train. The model domain represented the SCS geometry using a circular basin (purple dashed line in Fig. 1). Since the eddy train in NSCS existed mainly in the upper ocean over the deep water (>2000 m; Fig. 2) away from the bottom topography, we adopted a flat bottom with a bottom depth 2000 m. It had two straits in the northeastern and southeastern boundary to represent LS and southern passages (MS and KS). The model used a uniform horizontal rectangular grid with a grid size of 10 km. We adopted stretched generalized terrain-following coordinates (s) (Song and Haidvogel 1994) in the vertical. The model had 30 vertical levels, and we used $\theta_s = 3$ and $\theta_b = 0.985$ in s , where θ_s and θ_b are the surface and bottom control parameters, to represent higher vertical resolution in the surface and bottom boundary layers, respectively. We used temperature (T) and salinity (S) annual mean data from World Ocean Atlas to initialize the model. The temperature and salinity data were horizontally uniform, which may suppress the baroclinic instability, in order to better extract the dominant forcing process invoked in the eddy train. For simplicity, we set the buoyancy flux from the atmosphere to zero, and we set

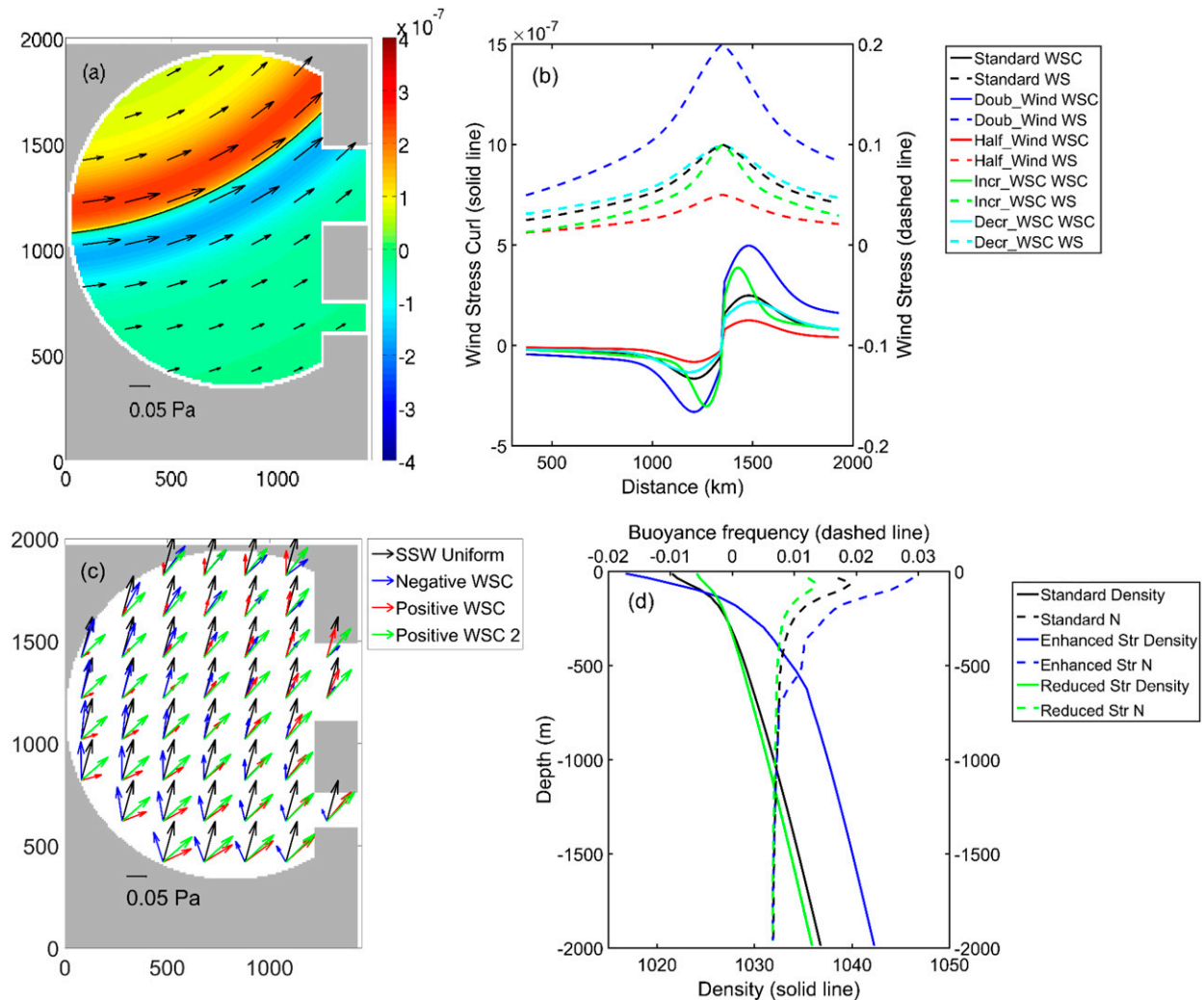


FIG. 5. (a) Wind stress (WS, Pa) vectors with the zero WSC line (black line) in the standard case. The color contours show the WSC (Pa m^{-1}); (b) WS and WSC in the north-south section that crosses the basin center. Doub_Wind/Half_Wind: wind forcing (including the WS and WSC) is twice/half that of the standard case. Incr_WSC/Decr_WSC: WSC is increased/decreased. (c) Spatially uniform SSW wind forcing (black arrow) and wind forcing with uniform WSC (blue arrow: $-1.1 \times 10^{-7} \text{ Pa m}^{-1}$, red arrow: $9.8 \times 10^{-8} \text{ Pa m}^{-1}$, green arrow: $2.4 \times 10^{-8} \text{ Pa m}^{-1}$); (d) vertical profiles of density and buoyancy frequency N in the standard case and cases with enhanced/reduced stratification (Enhanced Str/Reduced Str).

the initial velocities and elevation to zero. We ran the model to conduct a base experiment (the standard case) and several sensitivity experiments.

For the standard case, we forced the model with a representative southwesterly monsoon wind that had a prevailing dipole WSC (Fig. 5a) to mimic mean summer wind forcing in the SCS. The WS along the zero WSC line was 0.1 Pa, and its magnitude decreased southward and northward from that line. The wind pattern is similar to those used in previous studies (Gan et al. 2006, 2016a; Wang et al. 2012) and the sensitivity tests showed that the eddy-train formation was not sensitive to the position of the zero WSC line. The standard case reproduced well the characteristics of the observed eddy train, as demonstrated in section 4.

To examine different dynamic forcing processes for the formation of the AEs, we conducted a suit of sensitivity experiments with different stratifications, wind forcing fields, and various external fluxes in the straits, representing typical forcing conditions in the SCS (e.g., Gan et al. 2016a). The sensitivity experiments and their forcings are summarized in Table 1. In cases a1 and a2, the stratification in the water column was enhanced and reduced, respectively (Fig. 5d). In cases b1–b4, the wind patterns were the same as in the standard case, but with different magnitudes of WS and WSC (Fig. 5b). In cases d1–d4, we removed the dipole WSC and zero WSC line from the wind field to identify the effect on the jet separation, as a result of the Sverdrup effect, and on the

TABLE 1. Summary of sensitivity experiments. WS in the table represents the largest wind stress in the basin. The N values are the buoyancy frequency averaged over the upper 200 m.

Case	WS	WSC	Zero WSC line	Stratification	Inflow/outflow
Standard case	0.1 Pa	Normal, dipole	Yes	Normal N 0.016	5 Sv
a1	0.1 Pa	Normal, dipole	Yes	Enhanced N 0.024	5 Sv
a2	0.1 Pa	Normal, dipole	Yes	Reduced N 0.012	5 Sv
b1	Double	Double, dipole	Yes	Normal	5 Sv
b2	Half	Half, dipole	Yes	Normal	5 Sv
b3	0.1 Pa	Increased, dipole	Yes	Normal	5 Sv
b4	0.1 Pa	Decreased, dipole	Yes	Normal	5 Sv
c1	0.1 Pa	Normal, dipole	Yes	Normal	15 Sv
c2	0.1 Pa	Normal, dipole	Yes	Normal	1 Sv
d1	0.1 Pa	0	No	Normal	5 Sv
d2	0.1 Pa	Negative, $-1.1 \times 10^{-7} \text{ Pa m}^{-1}$	No	Normal	5 Sv
d3	0.1 Pa	Positive 1, $9.8 \times 10^{-8} \text{ Pa m}^{-1}$	No	Normal	5 Sv
d4	0.1 Pa	Positive 2, $2.4 \times 10^{-8} \text{ Pa m}^{-1}$	No	Normal	5 Sv

eddy-train formation. Similarly, in the d1–d4 cases, we applied spatially uniform south-southwesterly (SSW) WS (0.1 Pa) and wind forcing with negative/positive WSC ($-1.1 \times 10^{-7} \text{ Pa m}^{-1}$, $9.8 \times 10^{-8} \text{ Pa m}^{-1}$, and $2.4 \times 10^{-8} \text{ Pa m}^{-1}$), respectively (Fig. 5c).

The mean magnitude of the westward transport through LS ranges from 3 to 6.5 Sv ($1 \text{ Sv} \equiv 10^6 \text{ m}^3 \text{ s}^{-1}$; Hsin et al. 2012). We adopted 5 Sv as the transport for all the experiments based on the recent finding by Gan et al. (2016a). The exceptions were cases c1 and c2, for which we set the volume transport as 15 Sv and 1 Sv, respectively, to explore the effect of external flux on eddy-train formation.

We used the active open boundary conditions (OBCs) developed by Gan and Allen (2005) to integrate the external barotropic flux through the straits. The OBCs separate model variables at the open boundary into a forced local part and an unforced global part, such that the unforced radiation open boundary condition can be applied to the global part. We made the local part of the barotropic velocity ϕ_l horizontally uniform and calculated the barotropic velocity from the volume transport using Gan et al.'s (1997) method: $\phi_l = Q / \sum [h(y) \Delta y]$, where Q is the volume transport normal to the open boundary, $h(y)$ is the water depth along the boundary, and Δy is the meridional grid spacing. We used the modified Orlanski implicit radiation boundary condition (Camerlengo and O'Brien 1980) to compute the baroclinic velocity, and we imposed the advection boundary condition to T and S after making the initial T and S external values. We applied a no-gradient condition to the surface elevation along the open boundaries. A harmonic viscosity with a constant eddy coefficient ($5 \text{ m}^2 \text{ s}^{-1}$) represented the horizontal diffusion. We used the 3-day-averaged model output for our analyses.

4. Formation of the eddy train

In the standard case, the wind forcing generated a northward western boundary current in the upper layer (200 m). The current separated from the western boundary near the zero WSC line and formed a relatively weak anticyclonic recirculation on day 30 (Figs. 6a,d). The recirculation, our first simulated AE, resembled the observed eddy E1 (Fig. 3). The northeastward separated jet along the zero WSC was generally weak. We used the Okubo–Weiss parameter W (Wang and Gan 2014) to calculate the radius of the simulated eddies. The core radius of the first AE was 55 km, and the mean vorticity within the core was $-4.5 \times 10^{-6} \text{ s}^{-1}$ on day 30.

After initial onset, the separated jet strengthened, and the first AE deepened and produced a new eddy on day 60 that was east of the first one (Figs. 6b,e). The radius and mean vorticity of the first AE increased to 109 km and $-5.0 \times 10^{-6} \text{ s}^{-1}$, and the second AE had a radius and mean vorticity of 54 km and $-3.6 \times 10^{-6} \text{ s}^{-1}$. By day 90, a third AE formed east of the second one along the meandering jet while the first two AEs strengthened (Figs. 6c,f). These three AEs evolved into an eddy train along the separated jet. At this point, the radius of the first, second, and third eddies are 135, 82, and 50 km, and their mean vorticities are -5.8×10^{-6} , -5.5×10^{-6} , and $-4.0 \times 10^{-6} \text{ s}^{-1}$, respectively.

The spatiotemporal evolution of the AEs in Fig. 7 shows that the AEs formed sequentially from west to east while the intensity and size of these eddies in the eddy train decreased from west to east. Driven by constant wind forcing, the AEs propagated slowly because of the stationary boundary current separation and separated jet (see section 5a).

The eddies' strength decreased with depth. The vertical extensions of the AEs decreased from the west to the east,

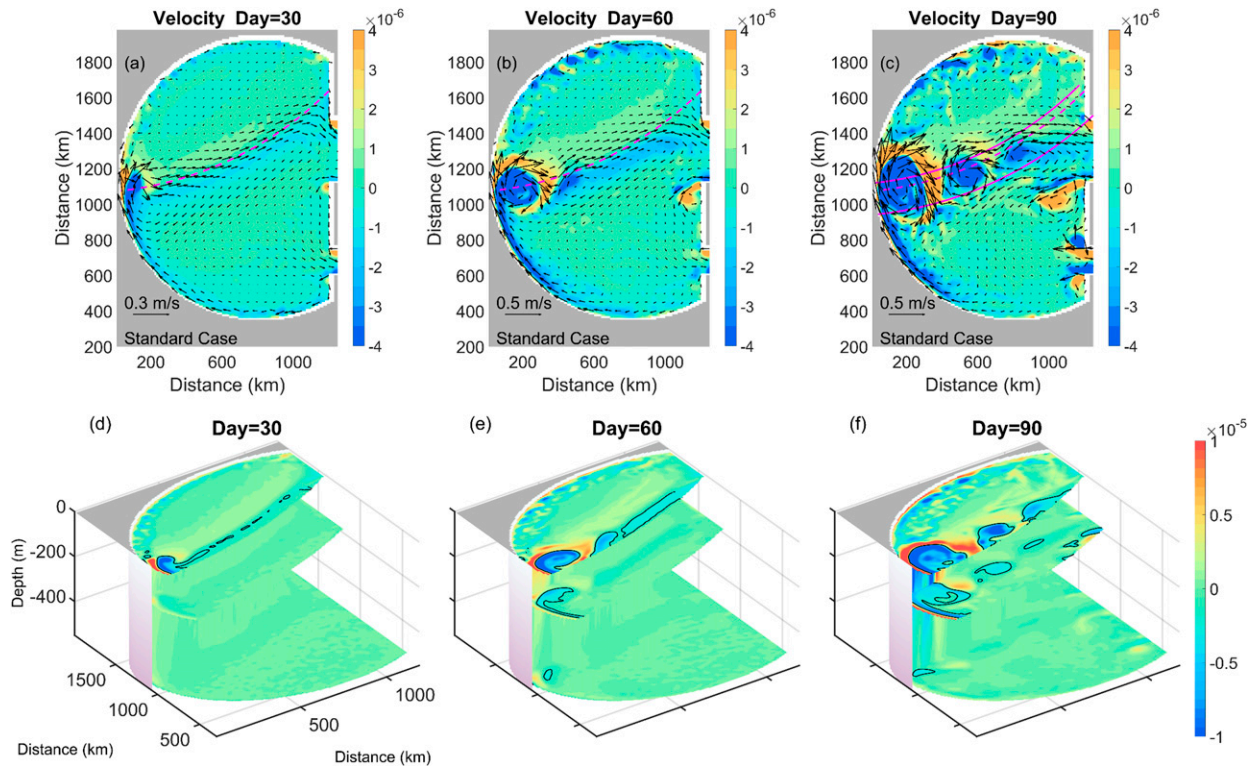


FIG. 6. (a)–(c) Surface velocity vectors (m s^{-1}) and vorticity (color contours; s^{-1}) averaged over the upper 200 m in the standard case on days 30, 60, and 90. The purple dashed line indicates the position of the zero WSC. (d)–(f) Three-dimensional structure of vorticity during the formation of the eddy train in the standard case. The black line indicates relative vorticity equal to $-2 \times 10^{-6} \text{ s}^{-1}$. The region within the solid purple lines is defined as the band of the eddy train.

but increased with time (Figs. 6d–f and Fig. 7b), subject to the eddies’ intensities. Before day 40, the single AE was mainly trapped near the surface (Figs. 6d and 7b). Then the AEs extended downward and the vertical gradient of vorticity weakened during formation. By day 90, the first AE reached $\sim 500\text{ m}$ while its intensity became its strongest with a vorticity equal to $-6.1 \times 10^{-6} \text{ s}^{-1}$ at the surface and more than $-0.5 \times 10^{-6} \text{ s}^{-1}$ at 500 m (Fig. 7b). The negative vorticity decayed mainly within the upper 300 m, where the buoyancy frequency was relatively large (Fig. 5d). The positive vorticity below 1000 m was located mainly along the cyclonically southward-moving boundary current at the depths.

Our process-oriented model well produced qualitatively the observed boundary current separation and separated jet, and as a result, it also well captured the observed formation and evolution processes of the eddy train (section 2). In particular, the simulated AEs were

south of the separated jet and stationary, and the westernmost eddy was induced by boundary current separation. We noticed that some of the AEs crossed the zero WSC line to reach the region of positive WSC (Figs. 6a–c). Although the current rotated cyclonically between the AEs (Fig. 6), no cyclonic eddy formed. The consistency between the simulated and observed eddy trains made us confident in the dynamic capabilities of our model.

5. Discussion

a. Vorticity balance in the eddy train

We illustrate the underlying dynamics of the eddy train’s formation with the analyses of the vorticity balance. We averaged the vorticity balance equation over the upper 200 m, where the AEs primarily existed:

$$\underbrace{\frac{\partial \bar{\xi}}{\partial t}}_{\text{VOR_ACCE}} = \underbrace{-\nabla \cdot \nabla \bar{\xi}}_{\text{VOR_HADV}} - \underbrace{\nabla \times \left(\overline{W \frac{\partial \mathbf{V}}{\partial z}} \right)}_{\text{VOR_VADV}} - \underbrace{(f + \bar{\xi}) \nabla \cdot \mathbf{V}}_{\text{VOR_DIV}} - \underbrace{\beta \bar{v}}_{\text{VOR_}\beta} + \nabla \times \left(\frac{\bar{\tau}_s}{\rho_0 D} - \frac{\bar{\tau}_b}{\rho_0 D} \right), \quad (1)$$

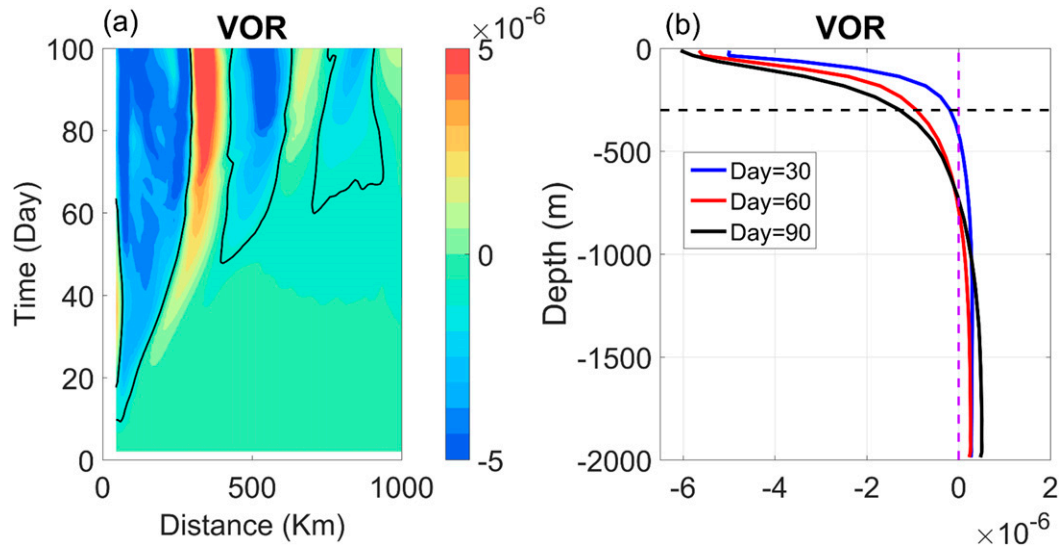


FIG. 7. (a) Time series of vorticity (s^{-1}) as a function of distance along the eddy train for the standard case. The vorticity was averaged over the upper layer ($<200\text{ m}$) along the eddy train between the purple lines shown in Fig. 6c. The black contour line indicates vorticity equal to $-1 \times 10^{-6} \text{ s}^{-1}$. (b) Vertical structure of vorticity (s^{-1}) averaged within the region of the first AE in the eddy train on days 30, 60, and 90 for the standard case. The black dashed line depicts 300 m depth.

where ξ is the relative vorticity. Here, \mathbf{V} is the vector form of the horizontal velocity, W is the vertical velocity, and v is the meridional component of velocity; β is the meridional gradient of the Coriolis parameter. The variables τ_s and τ_b are the stresses at the surface and bottom of the layer. The reference density and the layer depth are represented by ρ_0 and D ; t and z donate the derivative in time and vertical direction. The term on the lhs is the curl of the acceleration. The first four terms on the RHS are the horizontal vorticity advection, curl of vertical advection, the divergence term, and the beta effect. The last term in the equation is the curl of vertical viscosity, represented by the net surface and bottom stress curls. The horizontal viscosity term was much smaller compared to the other terms. The overbar means that the term was depth averaged.

Figures 8 and 9 illustrate the evolution of vorticity balance during the eddy-train formation for the standard case. The figures show the dominant terms in Eq. (1) on day 60, when the second eddy was forming and the first eddy was growing.

The horizontal advection of vorticity (VOR_HADV) and the impact of the beta effect on the fluid motion (VOR_BETA) may explain the increase of negative vorticity in the eddy train. In other words, the advection of preexisting vorticity by the current or the latitudinal advection of fluid parcel induce a negative vorticity flux in the location of the first AE (Fig. 8). Water converged within the first eddy and contributed negatively to the eddy's growth (positive VOR_DIV), although mass convergence geostrophically favored the eddy's maintenance. The magnitude of the vertical advection (VOR_VADV) was relatively small.

For the second AE, horizontal advection and the beta effect provided the negative vorticity (Fig. 8). The first eddy strengthened the intensity of the nearby northeastward separated jet. The jet produced a stronger negative shear velocity and transported the vorticity downstream to form the second AE subsequently. Same as the first AE, the advection of preexisting vorticity by the current or the latitudinal advection of the fluid parcel contribute negative vorticity to this eddy. The position and strength of the first eddy and jet controlled the location of the second eddy. The third AE formed in a similar fashion to the second one.

Negative WSC provided the favorable condition for forming all three AEs, but it was not the major cause for them compared to horizontal advection and the beta effect. The horizontal advection and beta effect were why the AEs can cross the zero WSC line (Fig. 6) and exist in a region with positive WSC. It is conceivable that the dipole WSC affected the AEs' formation by regulating the jet separation instead of directly providing vorticity for the eddy train.

Figure 9 contains the time series of the dominant terms in Eq. (1) as a function of distance along the eddy train. While the eddy train was forming, the vorticity acceleration (VOR_ACCE) was controlled by VOR_HADV and VOR_BETA. Unlike net effect averaged over the entire eddy in Fig. 8, the spatial distribution of the terms in Fig. 9 revealed that the horizontal advection/beta effect was always positive/negative west of the eddy and was negative/positive east of the eddy, as a result of the current direction and vorticity distribution of the eddy (Fig. 8a).

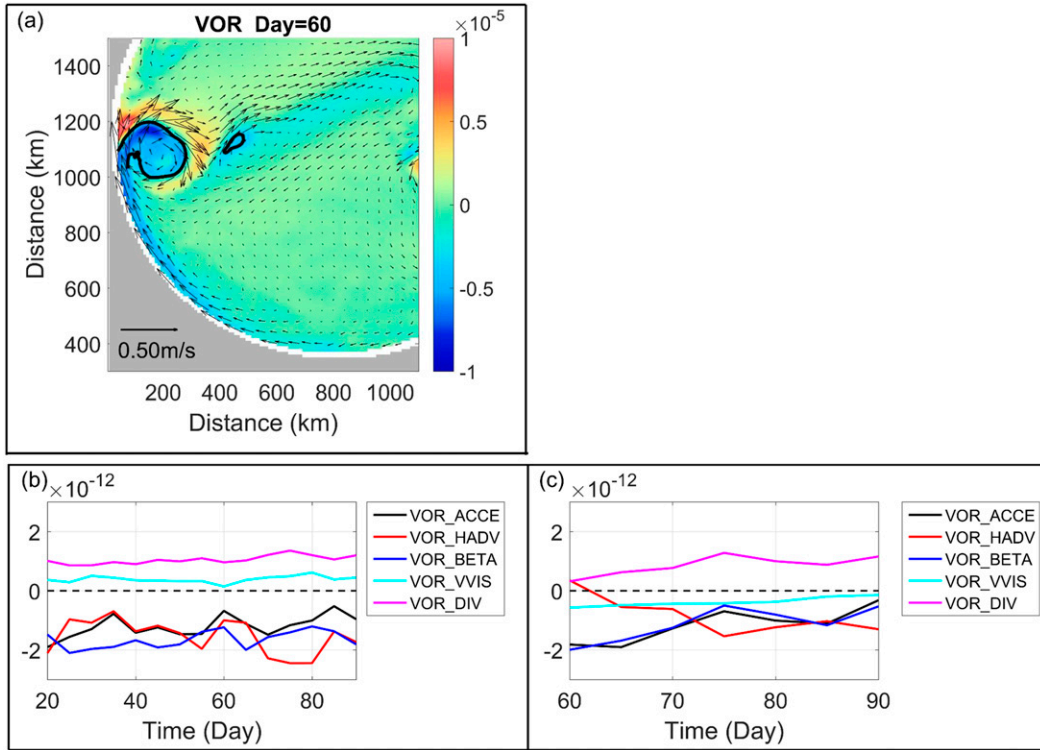


FIG. 8. (a) Surface velocity vectors (m s^{-1}) and vorticity (color contours; s^{-1}) in the standard case on day 60. The black circle refers to the relative vorticity equal to $-4 \times 10^{-6} \text{ s}^{-1}$ and shows the regions around the first and the second AEs. The time series of the major terms (s^{-2}) in the vorticity balance that were averaged within the (b) first and (c) second AE are defined by a black circle. VOR_ACCE, VOR_HADV, VOR_BETA, VOR_VVIS, and VOR_DIV indicate the vorticity acceleration, horizontal advection, beta, vertical viscosity, and divergence term, respectively.

Thus, the beta effect of the western boundary current provided negative vorticity for the first eddy in the eddy train and prevented the AEs from being destroyed by the upstream positive vorticity advection. Subsequently, the advection of negative vorticity in the separated jet provided vorticity to the AEs downstream of the train.

b. Vertical extent of the AEs in the eddy train

The Rossby number (HADV/COR) within the AE (Fig. 10) indicates that the geostrophic balance dominates the eddy current. Pressure gradient force (PGF) at the depth $-h$ can be divided into a barotropic part (BTPGF) and a baroclinic part (BCPGF):

$$\begin{aligned}
 \text{PGF} &= -\frac{1}{\rho_0} \nabla \left(\int_{-h}^{\eta} \rho g dz \right) \\
 &= -\frac{1}{\rho_0} \left(\underbrace{\rho_{z=\eta} g \nabla \eta}_{\text{BTPGF}} + \underbrace{\int_{-h}^{\eta} g \nabla \rho dz}_{\text{BCPGF}} \right), \quad (2)
 \end{aligned}$$

where η is sea surface elevation and ρ is the density. When the AE is forming, the BTPGF is induced by the

horizontal gradient of sea level in the eddy and is uniform in the water column. During the geostrophic adjustment in the eddy, the pressure field and velocity field in the ocean tend to mutually adjust toward a quasi-balance state, or thermal wind balance. Downwelling inside the AEs led the isopycnal surface to slant in the direction opposite to that of the sea level; thus, the BCPGF is the response to the surface water convergence/BTPGF. Figure 10 shows the depth dependence of the divergence of the pressure gradient force, $\nabla \cdot \text{PGF}$, $\nabla \cdot \text{BTPGF}$, and $\nabla \cdot \text{BCPGF}$ on day 90 when the first AE had its largest vertical extent. Near the surface, the $\nabla \cdot \text{BTPGF}$ dominated the $\nabla \cdot \text{PGF}$. It decreased from the surface to the bottom following the variation of the negative baroclinic effect ($\nabla \cdot \text{BCPGF}$). Therefore, with geostrophic balance, the baroclinicity of the eddy limits the vertical extent of the eddy through thermal wind relation, that is, $fV_{\eta} - fV_{-h} = \text{BCPGF}$, where V_{η} and V_{-h} are the magnitude of velocity at the surface and depth $-h$, respectively. In section 5c, we show that the enhanced stratification led to a faster vertical decay of vorticity due to the strengthened BCPGF, even when the AE was relatively strong in the surface layer.

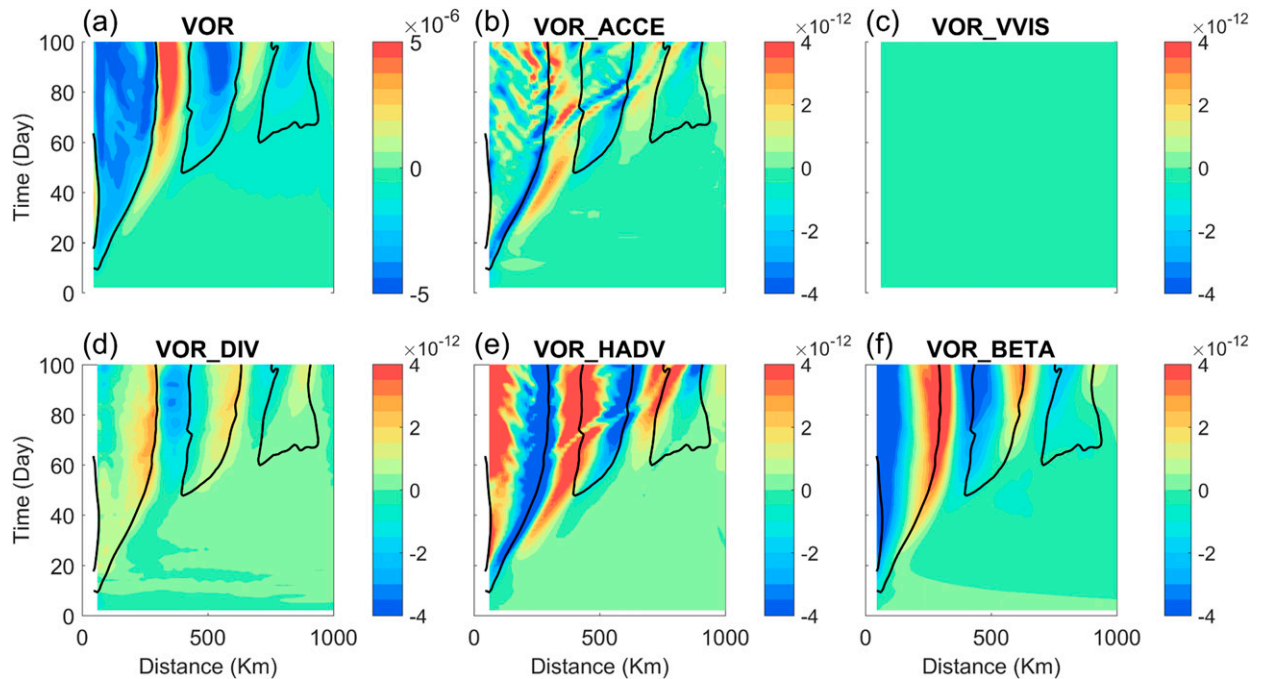


FIG. 9. Time series of (a) vorticity (s^{-1}) and (b)–(f) dominant terms (s^{-2}) in the vorticity equation as function of distance along the band of the eddy train in standard case. The black line shows the position of vorticity equal to $-1 \times 10^{-6} s^{-1}$.

The sum of the Coriolis term (COR) and PGF in the balance of momentum is referred to as the ageostrophic term (AGE; Gan and Allen 2005). The magnitude of the AGE is one order smaller than the COR and PGF terms. The net contribution of the $\nabla \cdot \text{COR}$ provided the negative $\nabla \cdot \text{AGE}$ in the upper layer, which was balanced mainly by the nonlinear effect ($\nabla \cdot \text{HADV}$; Fig. 10). The nonlinear term included the effect of centripetal acceleration due to the curvature associated with anticyclonic circulation within the eddy. The effect of the vertical viscosity ($\nabla \cdot \text{VVIS}$) was much smaller and confined to the upper and bottom boundary layers.

c. Role of stratification, wind forcing, and influx from strait

The basin circulation and boundary current separation, which control the formation of a long-lived eddy train, can be affected by a variety of forcings. Stratification affects the intensity of upper-basin circulation and the strength of the baroclinicity in the water column. Wind forcing, including WS and WSC, drives the basin circulation and boundary current separation. In addition, influx from straits also provides vorticity for the formation of basin circulation (Gan et al. 2016b).

We conducted sensitivity experiments with different stratification (cases a1 and a2), wind forcing (cases b1–b4), and external fluxes through straits (cases c1 and

c2) to illustrate the role of the different forcings in the formation of eddy trains. Results show that, although the eddy train can be formed in all these cases, the number and three-dimensional structures of the AEs are different. We compared the results from the sensitivity experiments to the standard case results on day 90 when the three AEs formed and the first AE had the largest vertical extent. Horizontally, we averaged the upper layer (<200 m) vorticity along the band of eddy train as defined in Fig. 6c (Fig. 11). To get the vertical profile, we averaged the vorticity within the region of the first AE in the eddy train.

1) STRATIFICATION

The stratification was enhanced/weakened in case a1/a2, which illustrated how stratification affected the formation of the eddy train and the spatial characteristics of the AEs. The strengthened stratification in case a1 increased the intensity and horizontal extension of the eddies and enlarged their spatial scales compared to the eddies in the standard case (Fig. 11a). As a result of the strengthened stratification, the basin could not accommodate the third eddy so that there were only two eddies in the eddy train. The reduced stratification in case a2 produced smaller and weaker AEs, and there was no sufficient eddy source upstream for the formation of the third eddy.

Vertically, the negative vorticity quickly decayed in the upper 300 m in all cases (Fig. 12). Because of physical

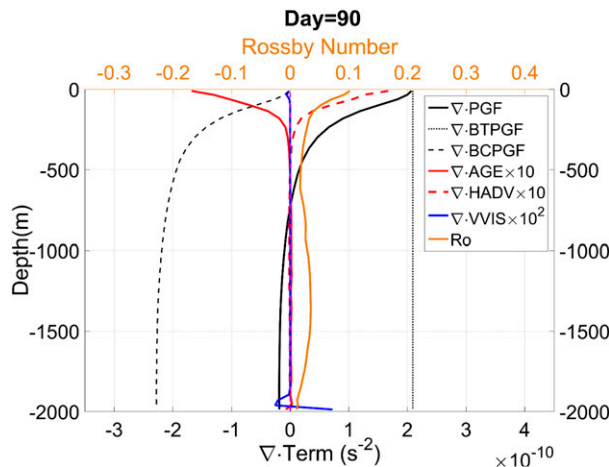


FIG. 10. The vertical structure of the divergence of the pressure gradient force ($\nabla \cdot \text{PGF}$), the barotropic part of the pressure gradient force ($\nabla \cdot \text{BTPGF}$), the baroclinic part of the pressure gradient force ($\nabla \cdot \text{BCPGF}$), the ageostrophic pressure gradient force ($\nabla \cdot \text{AGE}$), the horizontal advection ($\nabla \cdot \text{HADV}$), vertical viscosity ($\nabla \cdot \text{VVIS}$), and Rossby number (Ro) averaged within the region of the first AE in the eddy train on day 90 for the standard case.

insulation by stratification in the water column, the AE with the enhanced stratification did not extend as deeply as the AEs in the standard case and in case a2, even though the eddy caused by enhanced stratification had a stronger surface vorticity.

The AEs in the eddy train formed and grew mostly because of horizontal advection (VOR_HADV). The VOR_HADV from the first eddy was the source of vorticity for the second eddy, and, subsequently, for the

third one (section 5a). Therefore, we compared VOR_HADV in cases a1 and a2 to the advection in the standard case. Because not all sensitivity experiments generated a third AE on day 90, we chose the results on day 60 for our comparison. Day 60 was when the second AE formed (Figs. 13a,b).

The maximum velocity magnitudes in the band of eddy train are shown in Figs. 13c and 13d. The first two peaks of the maximum velocity magnitudes in the west represented the respective stronger current west and east of the first AE, which induced the third peak of the northeastward velocity in the second AE (see Fig. 8a). The third peak of the velocity magnitudes was just upstream of the negative VOR_HADV and formed a larger advection that generated the second AE in the eddy train in all cases. The enhanced stratification strengthened the jet current by confining the circulation to the upper layer, providing a larger horizontal vorticity advection to form larger and stronger AEs than those that occurred in the standard case (Figs. 13a,c). The enhanced stratification also induced a larger baroclinic deformation radius, and thus there existed only two eddies in the basins due to larger horizontal extension of the eddies (Fig. 11a). As also shown before, we found only two eddies in the eddy train from case a2. The first eddy was smaller and the second one was weaker with the reduced stratification. The smaller and weaker eddies were clearly due to a weakened jet current and corresponding vorticity advection and smaller deformation radius (Figs. 13b,d).

Vertically, the geostrophic balance also dominated the AEs in cases a1 and a2. The vertical changes

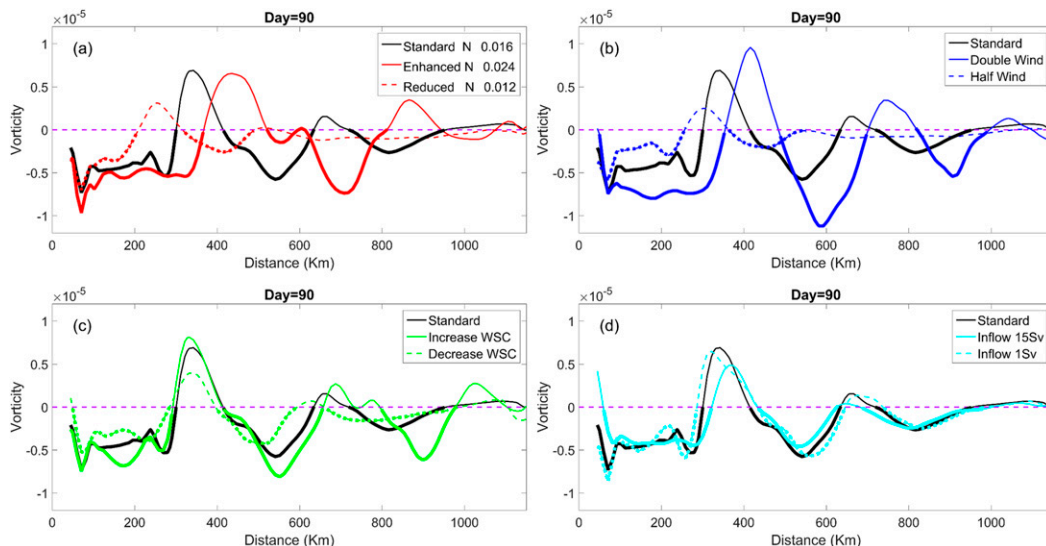


FIG. 11. Vorticity (s^{-1}) averaged in the upper 200 m along the band of eddy train with different strengths of (a) stratification, (b) wind forcing, (c) WSC, and (d) inflow on day 90. The N values are the buoyancy frequency averaged in the upper 200 m. Bold lines indicate the regions with AEs.

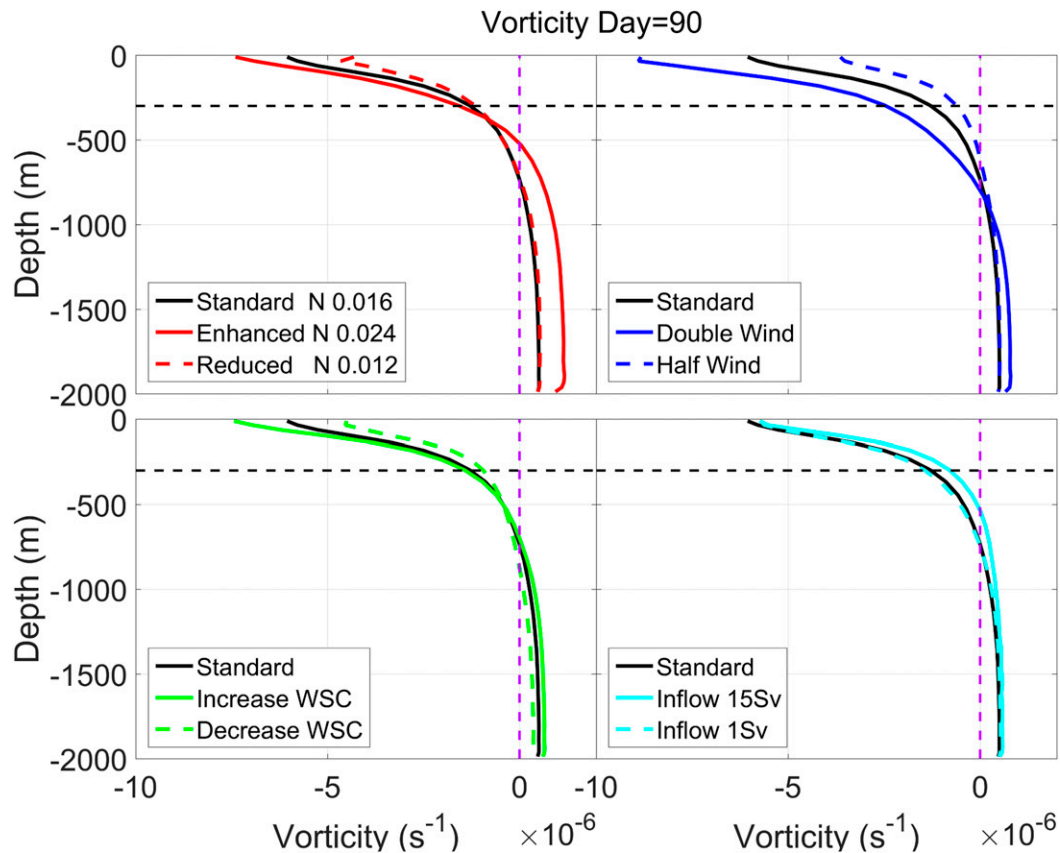


FIG. 12. The vertical structure of the vorticity (s^{-1}) averaged within the region of the first AE in the eddy train on day 90 for different cases. The black dashed line depicts 300 m depth.

of $\nabla \cdot \text{PGF}$ (Fig. 14a) were consistent with the vorticity (Fig. 12). The upper negative $\nabla \cdot \text{AGE}$ was balanced mainly by the nonlinear effect ($\nabla \cdot \text{HADV}$). The enhanced stratification led to the faster vertical decay of the AE because of the larger BCPGF. The enhanced stratification also weakened the vertical viscosity divergence ($\nabla \cdot \text{VVIS}$) in the upper layer. On the contrary, the reduced stratification caused a slower vertical decay of the first eddy. The influence of the vertical viscosity ($\nabla \cdot \text{VVIS}$) was relatively stronger in case a2 than in the standard case, but was still quite small compared with the other terms.

2) WIND FORCING

Summer monsoon wind forcing was a favorable factor in forming eddies. The wind intensified the western boundary current and the separation of the jet. With twice the prevailing summer wind forcing (both WS and WSC are doubled) in case b1, the strength and size of the AEs were larger than the AEs from the standard case (Fig. 11b). Unlike case a1, which had normal wind forcing but enhanced

stratification, there were three AEs in the eddy train in case b1. The difference between cases a1 and b1 indicates that stratification played a more important role in the spatial scale of the AEs in an eddy train than wind forcing. For case b1, the AEs were located farther downstream because of the stronger jet. With half the wind forcing (case b2), the strength and size of the first and the second AEs were much smaller, and the third AE did not form because there was not enough downstream vorticity advection.

In cases b3 and b4, the WSC was increased and decreased while the WS was slightly decreased and increased relative to the standard case, respectively. For case b3, with a larger WSC and weaker WS, the AEs were stronger and larger than the AEs from the standard case (Fig. 11c). In case b4, with smaller WSC and stronger WS, the AEs were weaker and smaller than the AEs from the standard case. The comparison of b3 and b4 clearly shows that the WSC played a more significant role than the WS in the strength of the AEs in the eddy train.

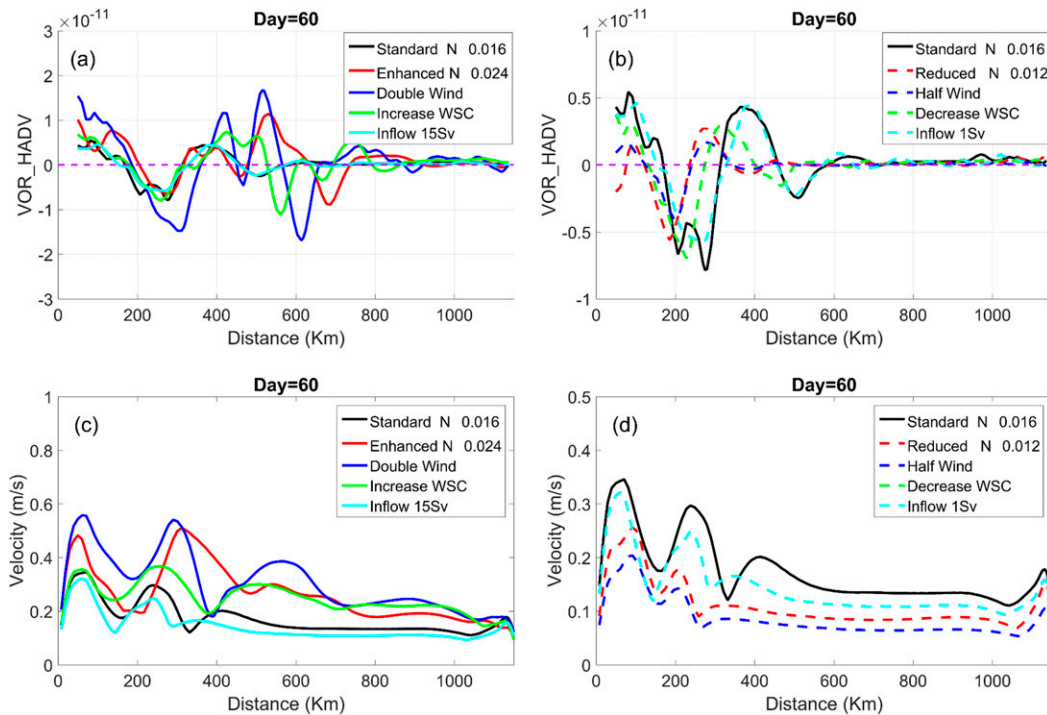


FIG. 13. (a),(b) Horizontal vorticity advection (VOR_HADV ; s^{-2}) averaged along the band of the eddy train, and (c),(d) maximum velocity magnitude ($m\ s^{-1}$) along the band of the eddy train as a function of distance on day 60 for different cases.

The vertical structures of vorticity in the AEs in cases b1–b4 were similar to the vertical structures in the standard case. The major difference was in the intensity of the eddies. Double/half wind forcing had the strongest/weakest surface vorticity (Fig. 12). Like stratification, wind forcing (WS and WSC) affected the intensity of the AEs by changing the intensity of the separated jet. The cases with double wind forcing and increased WSC (cases b1 and b3) generated a stronger jet than the standard case generated and provided larger horizontal vorticity advection for the formation of larger and stronger AEs (Figs. 13a,c). In contrast, the AEs were smaller and weaker in cases b2 and b4 (Figs. 11b,c).

Vertically, the basic momentum balances of the AEs in cases b1–b4 were the same as in the standard case. The baroclinic effect led to the vertical decay of the AEs. The case with double the wind forcing had the largest divergences of the nonlinear effect (Fig. 14c) and the larger vertical viscosity (Fig. 14d), but the AE in this case still extended to the deepest ocean because of its strong surface intensity.

3) INFLUX FROM STRAIT

The AEs in the eddy train weakened when the inflow/outflow in the straits increased from 5 to 15 Sv, but the

effect of the changing flux on the eddy train was limited (Fig. 11d). Below the upper layer (e.g., below 200 m), the vorticity decayed faster when there was a larger inflow (case c1) than in the standard case (Fig. 12). With a smaller inflow (1 Sv), such as in case c2, the AEs' horizontal and vertical patterns were almost the same as in the standard case.

The changes in lateral influx affected the background circulation, but the intensity of the western boundary current, the dipole WSC structure, and the stratification mainly controlled the western boundary current separation in the upper layer, which was the key forcing of the AEs. The effect of the lateral influx on the eddy train in the upper layer was limited compared to the other forcing factors (Fig. 13). The changes in the influx also had a limited effect on the vertical distribution of the AEs (Fig. 12).

d. Role of the jet separation

In section 5a, we showed the importance of the boundary current separation in forming the eddy train. To illustrate the role of the jet separation, we removed the dipole WSC in cases d1–d4. In these four cases, there was no separation of the jet, according to the Sverdrup theorem, and the current attached to the coast. There was no eddy train across

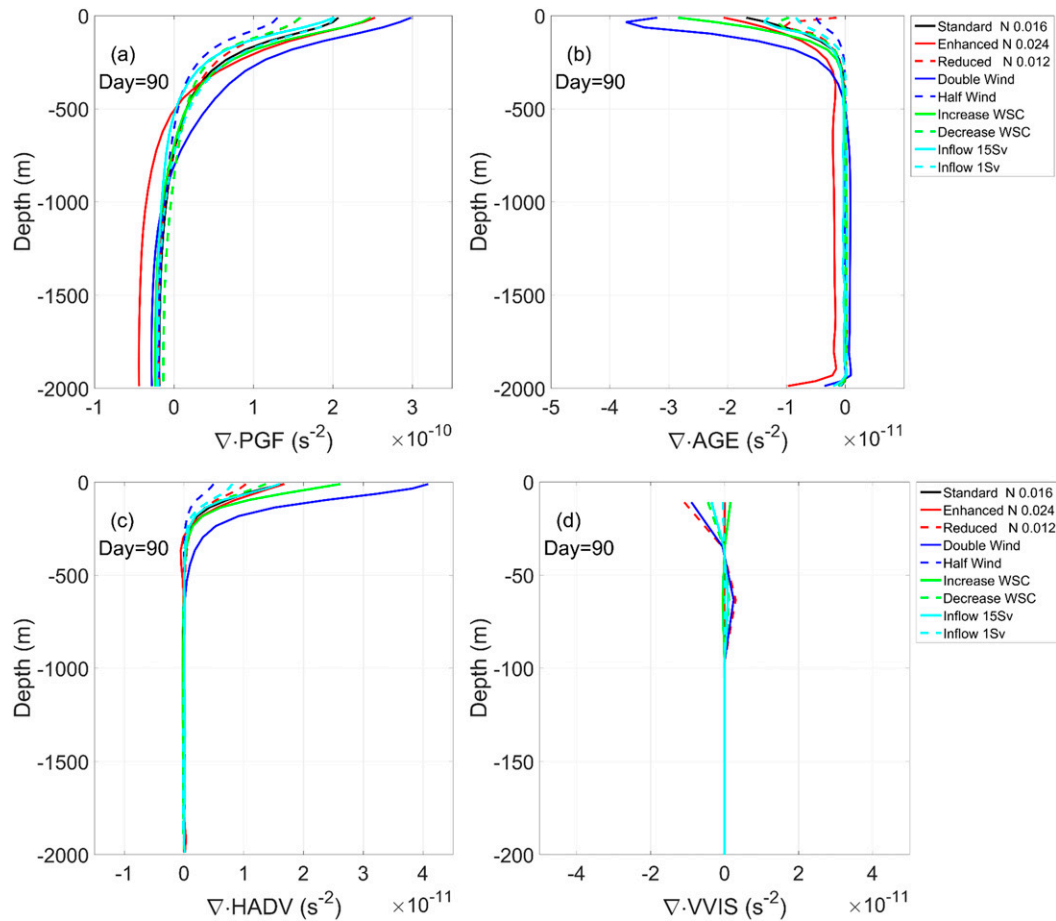


FIG. 14. The vertical structure of divergence of PGF, AGE, HADV, and VVIS (s^{-2}) averaged within the region of the first AE in the eddy train on day 90 for different cases.

the basin and if AEs were generated, they were along the boundary current. Case d1 was driven by a spatially uniform SSW WS (zero WSC in the entire basin), and the AEs formed right (with negative shear vorticity) of the boundary current axis (Fig. 15a). Case d2 had a negative WSC and a strong SSW WS in the western part of the basin, and a stronger northward western boundary current and AEs were produced (Fig. 15b) because of the negative vorticity from the WSC. There were more than three AEs along the boundary current in case d2. We forced case d3 with a positive WSC with a strong southwesterly WS in the southern part of basin, and the western boundary current flowed southward without any eddy forming (Fig. 15c). Case d4 had a weaker positive WSC, and the strong southwesterly WS overcame the effect of the weak positive WSC and drove the western boundary current to flow anticyclonically. In case d4, AEs were generated along the western boundary current, but they were much

weaker than the AEs that formed in cases d1 and d2 (Fig. 15d).

It is clear that if the jet did not separate, then the AEs could only exist in the jet along the western boundary. It is plausible that the northeastward vorticity advection in the separated jet formed the eddy train. The negative/positive WSC affected the basin circulation and strengthened/weakened the AEs. The shear vorticity of the northward boundary current favored AE formation, even when the WSC was positive.

In classical theory, the formation of the recirculation is part of the dynamics of the boundary current separation and the “adverse pressure gradient” is the key process governing the separation (Gan et al. 1997). Gan and Qu (2008) revealed that the adverse pressure gradient, balanced by the prevailing WS in summer, led to the coastal jet separation in the southwest SCS, as in cases d1, d2, and d4. The first AE naturally linked with the recirculation of the separation. Afterward, it evolved

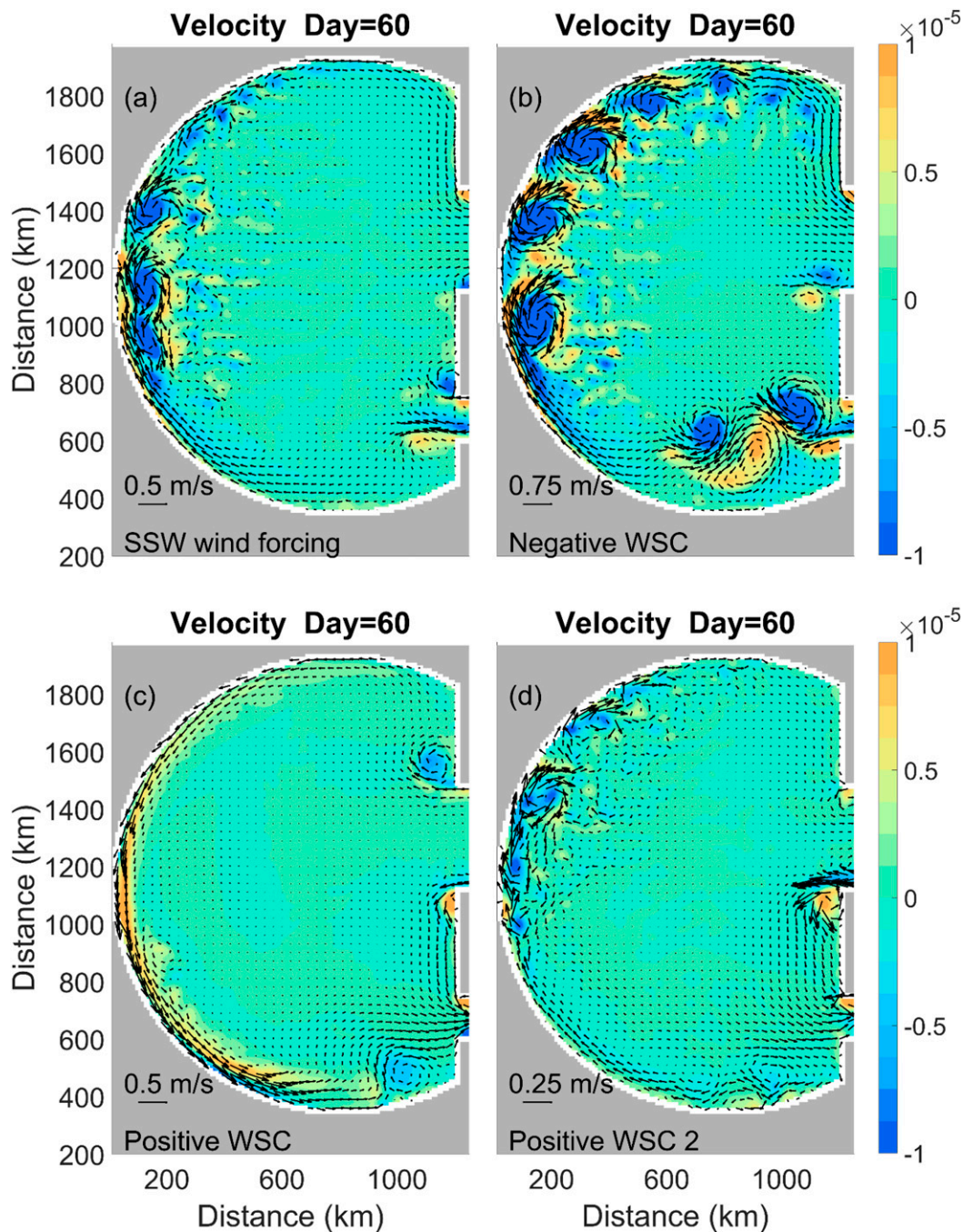


FIG. 15. The surface velocity vectors (m s^{-1}) and vorticity (color contours; s^{-1}) averaged over the upper 200 m in cases d1–d4 that were forced with (a) case d1, spatially uniform SSW WS; (b) case d2, negative WSC ($-1.1 \times 10^{-7} \text{ Pa m}^{-1}$); (c) case d3, positive WSC ($9.8 \times 10^{-8} \text{ Pa m}^{-1}$); and (d) case d4, positive WSC ($2.4 \times 10^{-8} \text{ Pa m}^{-1}$) for the entire domain on day 60.

into downstream AEs because of the negative vorticity input, due to vorticity advection, as in our standard case (Fig. 8). The WSC mainly influenced the basin circulation, and thus an AE could generate even with a weak positive WSC (case b4). But without the regulation of

the dipole WSC for the northeastward separation, an eddy train across the entire basin would not occur. In case d3, with strong positive WSC, the basin circulation reversed to flow cyclonically, and there was no coastal separation for AEs to form.

6. Summary

The long-lived eddy train across the SCS basin was frequently observed during summer. The eddy train played a critical role in regulating the circulation in the NSCS and in the entire SCS basin. Yet, its formation mechanics and dynamics remained largely unknown. We investigated the underlying forcing mechanisms of the eddy train with a three-dimensional process-oriented modeling study.

Our simulations produced the following scenario as a standard case. Forced by the southwesterly monsoon with a prevailing dipole WSC in summer, a northward coastal jet separated from the western boundary of the basin near the zero WSC line and reached northeastward into the basin. An anticyclone recirculation or an AE accompanied the separation and located right of the separated jet. As the AE developed, the jet meandered downstream with a strong negative shear vorticity, and a second and a third AE formed along the jet's path. These AEs evolved into the eddy train. The size and strength of the AEs decreased from west to east, and the AEs aligned roughly with the separated jet. The current rotated cyclonically between adjacent AEs without forming cyclonic eddies. Vertically, the strength of the AEs decayed within the upper 300 m, where the buoyancy frequency was relative large, and the strongest AE extended to ~500 m. The basic characteristics of the eddy train in the model resembled those found in observations.

To identify the roles of the major forcings in the eddy train formation, we conducted a suite of dynamic sensitivity experiments. The separation of the western boundary current was the key in forming the eddy train. When attachment of the western boundary current occurred, AEs were generated by a wind-driven anticyclonic circulation only along the jet in the western boundary, and there no eddy train formed across the entire basin. Enhanced stratification and increased wind forcing were favorable conditions for forming eddies, and the stratification played a critical role in determining the spatial scale of the AEs in the eddy train. Stratification had a negative effect on the vertical extension of the AEs because of the enhanced baroclinicity. The lateral influx from the idealized strait had a limited effect on the eddy train.

The underlying dynamics of the eddy train's formation were illustrated by the analyses of the vorticity balance of the processes that linked the separated jet to the eddy train. Horizontal advection of relative vorticity and the beta effect controlled the vorticity in the eddy train. The advection, particularly the beta effect, in the northward western boundary current was the source of negative vorticity for the eddy train. The subsequent downstream advection of

relative vorticity and the beta effect in the separated jet provided the vorticity sequentially from the first AE through to the third one. Therefore, the persistent separation of the boundary current maintained the long-lived eddy train in the SCS. The WSC mainly regulated the large-scale basin circulation and initiated the separation of the western boundary current. It did not directly form the cross-basin eddy train. In this way the AEs could exist in a region with positive WSC with input of negative vorticity by advection.

The stratification and intensity of the wind forcing also greatly controlled the basin's circulation. The enhanced stratification and increased wind forcing strengthened the intensity of the separated jet, producing larger vorticity advection to form larger and stronger downstream AEs in the eddy train.

Vertically, the BCPGF worked to limit the vertical extent of the eddy. As a result, the inherent stratification in the SCS regulated the three-dimensional scale of the AEs and constrained the vertical extent of the AEs by weakening the geostrophic balance inside the AEs.

With our modeling study, we obtained the dynamic processes and provided a novel understanding of the formation and features of the eddy train often observed in the SCS. We also identified key forcing dynamics.

Acknowledgments. This research was supported by the National (China) Key Basic Research Development Program (2015CB954004), and Hong Kong Research Grant Council (GRF16204915, GRF16206516). We are grateful for the useful comments provided by two anonymous reviewers.

REFERENCES

- Badin, G., R. G. Williams, J. T. Holt, and L. J. Fernand, 2009: Are mesoscale eddies in shelf seas formed by baroclinic instability of tidal fronts? *J. Geophys. Res.*, **114**, C10021, doi:10.1029/2009JC005340.
- Blumberg, A. F., and G. L. Mellor, 1987: A description of a three-dimensional coastal ocean circulation model. *Three-Dimensional Coastal Ocean Models*, Coastal and Estuarine Sciences, Vol. 4, Amer. Geophys. Union, 1–16.
- Caldeira, R. M. A., A. Stegner, X. Couvelard, I. B. Araújo, P. Testor, and A. Lorenzo, 2014: Evolution of an oceanic anticyclone in the lee of Madeira Island: In situ and remote sensing survey. *J. Geophys. Res. Oceans*, **119**, 1195–1216, doi:10.1002/2013JC009493.
- Camerlengo, A. L., and J. J. O'Brien, 1980: Open boundary conditions in rotating fluids. *J. Comput. Phys.*, **35**, 12–35, doi:10.1016/0021-9991(80)90031-5.
- Chen, G., Y. Hou, X. Chu, P. Qi, and P. Hu, 2009: The variability of eddy kinetic energy in the South China Sea deduced from satellite altimeter data. *Chin. J. Oceanol. Limnol.*, **27**, 943–954, doi:10.1007/s00343-009-9297-6.
- , —, and —, 2011: Mesoscale eddies in the South China Sea: Mean properties, spatiotemporal variability, and impact on thermohaline structure. *J. Geophys. Res.*, **116**, C06018, doi:10.1029/2010JC006716.

- , J. Gan, Q. Xie, X. Chu, D. Wang, and Y. Hou, 2012: Eddy heat and salt transports in the South China Sea and their seasonal modulations. *J. Geophys. Res.*, **117**, C05021, doi:10.1029/2011JC007724.
- Cheng, X., and Y. Qi, 2010: Variations of eddy kinetic energy in the South China Sea. *J. Oceanogr.*, **66**, 85–94, doi:10.1007/s10872-010-0007-y.
- Chi, P. C., Y. Chen, and S. Lu, 1998: Wind-driven South China Sea deep basin warm-core/cool-core eddies. *J. Oceanogr.*, **54**, 347–360, doi:10.1007/BF02742619.
- Chu, X., H. Xue, Y. Qi, G. Chen, Q. Mao, D. Wang, and F. Chai, 2014: An exceptional anticyclonic eddy in the South China Sea in 2010. *J. Geophys. Res. Oceans*, **119**, 881–897, doi:10.1002/2013JC009314.
- Couvelard, X., R. M. A. Caldeira, I. B. Araujo, and R. Tome, 2012: Wind mediated vorticity-generation and eddy-confinement, leeward of the Madeira Island: 2008 numerical case study. *Dyn. Atmos. Oceans*, **58**, 128–149, doi:10.1016/j.dynatmoce.2012.09.005.
- Fang, G., Y. Wang, Z. Wei, Y. Fang, F. Qiao, and X. Hu, 2009: Interocean circulation and heat and freshwater budgets of the South China Sea based on a numerical model. *Dyn. Atmos. Oceans*, **47**, 55–72, doi:10.1016/j.dynatmoce.2008.09.003.
- Gan, J., and J. Allen, 2005: On open boundary conditions for a limited-area coastal model off Oregon. Part 1: Response to idealized wind forcing. *Ocean Modell.*, **8**, 115–133, doi:10.1016/j.ocemod.2003.12.006.
- , and T. Qu, 2008: Coastal jet separation and associated flow variability in the southwest South China Sea. *Deep-Sea Res. I*, **55**, 1–19, doi:10.1016/j.dsr.2007.09.008.
- , R. G. Ingram, and R. J. Greatbatch, 1997: On the unsteady separation/intrusion of the Gaspé Current and variability in Baie des Chaleurs: Modeling studies. *J. Geophys. Res.*, **102**, 15 567–15 581, doi:10.1029/97JC00589.
- , H. Li, E. Curchitser, and D. Haidvogel, 2006: Modeling South China Sea circulation: Response to seasonal forcing regimes. *J. Geophys. Res.*, **111**, C06034, doi:10.1029/2005JC003298.
- , Z. Liu, and L. Liang, 2016a: Numerical modeling of intrinsically and extrinsically forced seasonal circulation in the China Seas: A kinematic study. *J. Geophys. Res. Oceans*, **121**, 4697–4715, doi:10.1002/2016JC011800.
- , —, and C. Hui, 2016b: A three-layer alternating spinning circulation in the South China Sea. *J. Phys. Oceanogr.*, **46**, 2309–2315, doi:10.1175/JPO-D-16-0044.1.
- Gula, J., M. J. Molemaker, and J. C. McWilliams, 2015: Topographic vorticity generation, submesoscale instability, and vortex street formation in the Gulf Stream. *Geophys. Res. Lett.*, **42**, 4054–4062, doi:10.1002/2015GL063731.
- Hsin, Y.-C., C.-R. Wu, and S.-Y. Chao, 2012: An updated examination of the Luzon Strait transport. *J. Geophys. Res.*, **117**, C03022, doi:10.1029/2011JC007714.
- Hu, J., J. Gan, Z. Sun, J. Zhu, and M. Dai, 2011: Observed three-dimensional structure of a cold eddy in the southwestern South China Sea. *J. Geophys. Res.*, **116**, C05016, doi:10.1029/2010JC006810.
- , Q. Zheng, Z. Sun, and C. K. Tai, 2012: Penetration of nonlinear Rossby eddies into South China Sea evidenced by cruise data. *J. Geophys. Res.*, **117**, C03010, doi:10.1029/2011JC007525.
- Jia, Y., and E. P. Chassignet, 2011: Seasonal variation of eddy shedding from the Kuroshio intrusion in the Luzon Strait. *J. Oceanogr.*, **67**, 601–611, doi:10.1007/s10872-011-0060-1.
- Kawaguchi, Y., M. Itoh, and S. Nishino, 2012: Detailed survey of a large baroclinic eddy with extremely high temperatures in the western Canada Basin. *Deep-Sea Res. I*, **66**, 90–102, doi:10.1016/j.dsr.2012.04.006.
- Lin, X., C. Dong, D. Chen, Y. Liu, J. Yang, B. Zou, and Y. Guan, 2015: Three-dimensional properties of mesoscale eddies in the South China Sea based on eddy-resolving model output. *Deep-Sea Res. I*, **99**, 46–64, doi:10.1016/j.dsr.2015.01.007.
- Liu, Z., H. Yang, and Q. Liu, 2001: Regional dynamics of seasonal variability in the South China Sea. *J. Phys. Oceanogr.*, **31**, 272–284, doi:10.1175/1520-0485(2001)031<0272:RDOSVI>2.0.CO;2.
- McWilliams, J. C., 1985: Submesoscale, coherent vortices in the ocean. *Rev. Geophys.*, **23**, 165–182, doi:10.1029/RG023i002p00165.
- Mellor, G. L., and T. Yamada, 1982: Development of a turbulence closure model for geophysical fluid problems. *Rev. Geophys. Space Phys.*, **20**, 851–875, doi:10.1029/RG020i004p00851.
- Molemaker, J., J. McWilliams, and W. Dewar, 2015: Submesoscale instability and generation of mesoscale anticyclones near a separation of the California Undercurrent. *J. Phys. Oceanogr.*, **45**, 613–629, doi:10.1175/JPO-D-13-0225.1.
- Nan, F., Z. He, H. Zhou, and D. Wang, 2011a: Three long-lived anticyclonic eddies in the northern South China Sea. *J. Geophys. Res.*, **116**, C05002, doi:10.1029/2010JC006790.
- , H. Xue, P. Xiu, F. Chai, M. Shi, and P. Guo, 2011b: Oceanic eddy formation and propagation southwest of Taiwan. *J. Geophys. Res.*, **116**, C12045, doi:10.1029/2011JC007386.
- Qu, T., 2000: Upper-layer circulation in the South China Sea. *J. Phys. Oceanogr.*, **30**, 1450–1460, doi:10.1175/1520-0485(2000)030<1450:ULCITS>2.0.CO;2.
- , Y. T. Song, and T. Yamagata, 2009: An introduction to the South China Sea throughflow: Its dynamics, variability, and application for climate. *Dyn. Atmos. Oceans*, **47**, 3–14, doi:10.1016/j.dynatmoce.2008.05.001.
- Song, Y., and D. Haidvogel, 1994: A semi-implicit ocean circulation model using a generalized topography-following coordinate system. *J. Comput. Phys.*, **115**, 228–244, doi:10.1006/jcph.1994.1189.
- Steward, R. H., 2009: *Introduction to Physical Oceanography*. Orange Grove Books, 345 pp.
- Su, J., 2004: Overview of the South China Sea circulation and its influence on the coastal physical oceanography outside the Pearl River Estuary. *Cont. Shelf Res.*, **24**, 1745–1760, doi:10.1016/j.csr.2004.06.005.
- Sun, Z., Z. Zhang, W. Zhao, and J. Tian, 2016: Interannual modulation of eddy kinetic energy in the northeastern South China Sea as revealed by an eddy-resolving OGCM. *J. Geophys. Res. Oceans*, **121**, 3190–3201, doi:10.1002/2015JC011497.
- Wang, D., H. Xu, J. Lin, and J. Hu, 2008: Anticyclonic eddies in the northeastern South China Sea during winter 2003/2004. *J. Oceanogr.*, **64**, 925–935, doi:10.1007/s10872-008-0076-3.
- Wang, G., R. X. Huang, J. Su, and D. Chen, 2012: The effects of thermohaline circulation on wind-driven circulation in the South China Sea. *J. Phys. Oceanogr.*, **42**, 2283–2296, doi:10.1175/JPO-D-11-0227.1.
- Wang, L., and J. Gan, 2014: Delving into three-dimensional structure of the West Luzon Eddy in a regional ocean model. *Deep-Sea Res. I*, **90**, 48–61, doi:10.1016/j.dsr.2014.04.011.
- Wu, C.-R., and T.-L. Chiang, 2007: Mesoscale eddies in the northern South China Sea. *Deep-Sea Res. II*, **54**, 1575–1588, doi:10.1016/j.dsr2.2007.05.008.
- Xiu, P., F. Chai, L. Shi, H. Xue, and Y. Chao, 2010: A census of eddy activities in the South China Sea during 1993–2007. *J. Geophys. Res.*, **115**, C03012, doi:10.1029/2009JC005657.
- Xu, F.-H., and L.-Y. Oey, 2015: Seasonal SSH variability of the northern South China Sea. *J. Phys. Oceanogr.*, **45**, 1595–1609, doi:10.1175/JPO-D-14-0193.1.

- Xue, H., F. Chai, N. Pettigrew, D. Xu, M. Shi, and J. Xu, 2004: Kuroshio intrusion and the circulation in the South China Sea. *J. Geophys. Res.*, **109**, C02017, doi:[10.1029/2002JC001724](https://doi.org/10.1029/2002JC001724).
- Zhang, Z., W. Zhao, J. Tian, and X. Liang, 2013: A mesoscale eddy pair southwest of Taiwan and its influence on deep circulation. *J. Geophys. Res. Oceans*, **118**, 6479–6494, doi:[10.1002/2013JC008994](https://doi.org/10.1002/2013JC008994).
- , J. Tian, B. Qiu, W. Zhao, P. Chang, D. Wu, and X. Wan, 2016: Observed 3D structure, generation, and dissipation of oceanic mesoscale eddies in the South China Sea. *Sci. Rep.*, **6**, 24349, doi:[10.1038/srep24349](https://doi.org/10.1038/srep24349).
- , W. Zhao, B. Qiu, and J. Tian, 2017: Anticyclonic eddy sheddings from Kuroshio loop and the accompanying cyclonic eddy in the northeastern South China Sea. *J. Phys. Oceanogr.*, **47**, 1243–1259, doi:[10.1175/JPO-D-16-0185.1](https://doi.org/10.1175/JPO-D-16-0185.1).
- Zheng, Q., and Coauthors, 2014: Standing wave modes observed in the South China Sea deep basin. *J. Geophys. Res. Oceans*, **119**, 4185–4199, doi:[10.1002/2014JC009957](https://doi.org/10.1002/2014JC009957).